https://doi.org/10.5194/bg-2021-130
Preprint. Discussion started: 10 June 2021

Biogeosciences Discussions
Open Access

Sensitivity of biomass burning emissions estimates to land surface information

Makoto Saito[1*], Tomohiro Shiraishi[1], Ryuichi Hirata[1], Yosuke Niwa[1], Kazuyuki Saito[2], Martin Steinbacher[3], Doug Worthy[4], and Tsuneo Matsunaga[1]

[1]National Institute for Environmental Studies, 16-2 Onogawa, Tsukuba, Japan
[2]Japan Meteorological Agency, 1-3-4 Ote-machi, Chiyoda-ku, Tokyo, Japan
[3]Swiss Federal Laboratories for Materials Science and Technology, Ueberlandstrasse 129, CH-8600 Duebendorf, Switzerland
[4]Environment and Climate Change Canada, 4905 Dufferin Street, Toronto, Ontario Canada

Correspondence: M. Saito (saito.makoto@nies.go.jp)

Abstract. Emissions from biomass burning (BB) are a key source of atmospheric tracer gases that affect the atmospheric carbon cycle. We estimated four types of global BB emissions using a bottom-up approach and by combining the remote sensing products related to fire distribution with two aboveground biomass (AGB) and two land cover classification (LCC) distributions. The sensitivity of the estimates of BB emissions to the AGB and LCC data was evaluated using the carbon monoxide (CO) emissions associated with each BB estimate. We found a substantial spatial difference in CO emissions for both the AGB and LCC data, which resulted in a large (factor of approximately three) spread of estimates for the mean annual CO emissions. We simulated atmospheric CO variability using an atmospheric tracer transport model and the BB emissions estimates and compared it with ground-based and satellite observations. At ground-based observation sites during fire seasons, statistical comparisons indicated that the impact of differences in the BB emissions estimates on atmospheric CO variability was poorly defined in our simulations. However, when compared at the regional and global scales, the distribution of atmospheric CO concentrations in the simulations show substantial differences among the estimates of BB emissions. These results indicate that the estimates of BB emissions are highly sensitive to the AGB and LCC data.

1 Introduction

The majority of biomass burning (BB) is related to human activities, with only a small fraction caused by natural processes such as lightning (Seiler and Crutzen, 1980; Balch et al., 2017). Various agriculture and economic processes involve BB; e.g., clearing of forest and brush land for agricultural use, or controlling fuel accumulation in forests (Andreae, 1991). Such intensive activities have significant implications for changes in regional land cover from fire-resistant to fire-prone systems (Turetsky et al., 2015). Even in savanna where fire-adapted trees are dominant, frequent fires and/or an abrupt increase in fire intensity can result in ecosystem degradation with a subsequent reduction in woody biomass (Saito et al., 2014). Furthermore, BB is a significant source of trace gases and aerosol particles in the atmosphere (e.g., Bougiatioti et al., 2014; Pan et al., 2020). Water vapor and carbon dioxide (CO_2) are the primary products of the burning of organic materials. In addition, in incomplete combustion, various other compounds such as carbon monoxide (CO), methane (CH_4), nitrogen oxides, and ammonia

https://doi.org/10.5194/bg-2021-130
Preprint. Discussion started: 10 June 2021

are emitted from the fires (Andreae, 1991). Recent studies have shown that climate change associated with rising anthropogenic emissions of greenhouse gases might lead to an increase in fire frequency over some regions (e.g., boreal regions), and emissions of greenhouse gases from terrestrial biosphere due to enhancement of BB (Dutta et al., 2016; Hart et al., 2019).

The quantification of BB emissions is crucial to our understanding of the role of BB with respect to the global carbon cycle and its interaction with climate change. At present, several global BB emission inventories are available thanks to advances in satellite observation technology. The satellite remote sensing products for fires, such as fire radiative power, active fires, and burned area, have been used to develop inventories of BB emissions (e.g., Wiedinmyer et al., 2011; Kaiser et al., 2012; van der Werf et al., 2017). These inventories provide BB emissions covering a variety of temporal and spatial resolutions. However, estimates of annual greenhouse gas and aerosol particle emissions based on these inventories show significant differences of $1.5\times$ and $3.8\times$ for CO_2 and organic carbon, respectively, as well as variations in the spatiotemporal patterns of the emissions (Shi et al., 2015; Pan et al., 2020). These divergences mean that our ability to represent BB processes at the global scale remains limited, and a basic research question regarding which of the available estimates better represents BB emissions over regional and global scales remains to be answered. Consequently, there is further need for information related to the development of better estimates of BB emissions.

Our analysis of BB emissions inventories used a bottom-up approach and incorporated land surface information regarding vegetated biomass density and land cover classifications (LCC), information on fire events, and several parameters related to burning efficiency. Although the technique used for land use mapping have improved over recent decades (e.g., Popescu et al., 2011; Rodriguez-Galiano et al., 2012), differences of between 10% and 20% remain in estimates of regional carbon stocks based on different land surface maps (Mitchard et al., 2013), which can cause divergence in estimates of BB emissions. In this study, we aim to evaluate the sensitivity of estimates of BB emissions to land surface information and compare our findings with the newly proposed BB emissions estimates. A detailed description of our BB emissions estimates, as well as a broad summary of the comparison of our estimates with four published reference BB datasets covering CO_2 emissions, can be found in Shiraishi et al. (2021). This study takes an additional step towards evaluation of BB estimates in terms of atmospheric CO variability, which can be used as a tracer to investigate the transport of BB emissions (e.g., Chen et al., 2009; Mu et al., 2011), using independent reference data from ground-based and satellite observations of atmospheric CO concentrations.

2 Methods

2.1 Biomass burning estimates

This study expresses CO emissions from BB (E; g CO month^{-1}) at a grid (i) at a resolution of 500 m, and the LCC (j) in each month (k), using the burned area method (e.g., Michel et al., 2005; Mieville et al., 2010):

$$E_{i,k} = BA_{i,k} \cdot F_{i,k} \cdot EF_j, \tag{1}$$

$$F_{i,k} = BE_j \cdot \sum_{l=m+1}^{n} \left(AGB_i(1-BE_j)^{l-1}\right) \tag{2}$$

https://doi.org/10.5194/bg-2021-130
Preprint. Discussion started: 10 June 2021

where $BA, F, EF, BE, \text{and} AGB$ are the burned area (m^2), the flammable fuel (kg m^{-2}), the emission factor (g CO kg^{-1}), the burning efficiency (which ranges from 0 to 1), and the above-ground biomass (kg m^{-2}), respectively. The parameters m and n are the cumulative number of fire occurrences during the previous $(k-1)$ and current month k, respectively. Equation (2) represents decreases in F due to frequent fires in a year. The biomass density; i.e., flammable fuel, decreases with increasing fire occurrence l. Note that the largest values of E and F occur during the first fire event in a year, as shown in Eqs (1) and (2), then E and F decline as more fire events occur. AGB is reset to its original magnitude; i.e., before the fires, at the beginning of each year.

To determine the sensitivity of the BB emissions estimates to the land surface information used, we calculated E based on four scenarios that combined two types of LCC and two types of AGB data. The LCC maps derived from the Global Land Cover 2000 project (GLC2000) (Bartholomé and Belward, 2005) and the Moderate Resolution Imaging Spectroradiometer (MODIS) Land Cover Type (MCD12Q1) Version 6 (Sulla-Menashe et al., 2019) data products were used to classify the land cover types in each grid. The GLC2000 provides a global LCC map with 22 land cover types (Table A1) based on daily data from the VEGETATION sensor onboard the Satellite Probatoire de l'Observation de la Terre (SPOT-4) satellite. It covers 14 months from 1 November 1999 to 31 December 2000 with a 1-km spatial resolution. We also used the MCD12Q1 International Geosphere-Biosphere Programme (IGBP) legend as another LCC map. This product provides a global LCC map with 17 land cover types (Table A2) with a spatial resolution of 500 m and yearly temporal resolution after 2001. The AGB maps were obtained from two datasets: the GEOCARBON global forest biomass map (Avitabile et al., 2016) and the Globbiomass AGB map (Santoro, 2018). The GEOCARBON map is a combined AGB map based on two pan-tropical datasets published by Saatchi et al. (2011) and Baccini et al. (2012) with reference field data and biomass maps, and provides the global AGB map at a 1-km spatial resolution. The Globbiomass map is an AGB product based on satellite observations from the radar backscattered intensity recorded by the Phase Array-type band Synthetic Aperture Radar (PALSAR) instrument, which is onboard the Advanced Land Observing Satellite (ALOS), and the Advanced Synthetic Aperture Radar (ASAR) instrument operating at C-band, which is onboard the Environmental Satellite (Envisat) and uses LiDAR-based metrics and surface reflectances. This AGB product is produced by the European Space Agency (ESA) with a 25-m spatial resolution. These LCC and AGB maps were used in Eqs (1) and (2) by aggregating or disaggregating them to a spatial resolution of 500 m.

The BA was obtained from the MODIS Thermal Anomalies and Fire Daily (MOD14A1) Version 6 dataset (Giglio et al., 2016). MOD14A1 provides daily fire mask compositions at a 1-km resolution, and we used the low-, nominal-, and high-confidences fire classes (FireMask = 7, 8, and 9, respectively) to detect BA. If a 1-km resolution grid point showed a fire flag on a particular day, then the 4 surrounding sub-grids with a 500 m resolution, located within the original MOD14A1 grid, were assumed to have burned; that is, $BA_{i,k} = 250,000$ m^2. Fire occurrences over a grid i in a month k were not involved in BA in this study, but they vary E with changes of F in Eq. (2). The fire occurrences were determined by counting the number of discontinuities of fires in a month. This means that, if the FireMask shows flags for fires (FireMask = 7,8,9) continuously over a month, the fire occurrence was set to $l = 1$.

The EF for CO was derived from the study of van der Werf et al. (2017). They compiled an EF dataset for six biomes based on the studies of Andreae and Merlet (2001) and Akagi et al. (2011). For this study, we reallocated the EF to the 22 land cover types used in GLC2000 (Table A1) and the 17 LCC types used in MCD12Q1 (Table A2). In this process, we classified the globe into 14 regions (after Giglio et al. (2006) and van der Werf et al. (2017); Fig. A1), then the EF from the 6 biomes was adapted to the corresponding LCC types based on the location of the objective grid in a region. The BE was derived from the study by Mieville et al. (2010). As their LCC conformed to GLC2000 (Table A1), the BE values were assigned to 17 LCC types on the MCD12Q1 map (Table A2).

We hereafter refer to BB emissions estimates based on GLC2000 using Globbiomass and GEOCARBON as GlcGlob and GlcGeoc, respectively, and those based on MCD12Q1 using Globbiomass and GEOCARBON as McdGlob and McdGeoc, respectively (Table 1). We used E data that were aggregated onto a grid with a resolution of about 0.837 degree in the following analysis.

2.2 Atmospheric tracer transport model

We used the Non-hydrostatic ICosahedral Atmospheric Model (NICAM)-based Transport Model (NICAM-TM; Niwa et al., 2011) to simulate atmospheric CO concentrations in this study. NICAM has a unique characteristic in its dynamical core; i.e., a non-hydrostatic system in the flux form that guarantees the conservation of tracer mass (Satoh, 2002). NICAM implements this non-hydrostatic scheme using an icosahedral grid configuration.

NICAM-TM includes a module for the reaction processes among hydroxyl radical (OH) and CO, and the oxidation of CH_4 with OH, which yields CO, to simulate atmospheric CO variability (Niwa et al., 2020). We used atmospheric OH field data from the TransCom-CH_4 project (Patra et al., 2011). The atmospheric CH_4 concentration in the simulation was fixed at 1800 ppb. In this study, we used a globally uniform grid system with a horizontal resolution of about 220 km and 40 vertical layers. Horizontal winds in NICAM-TM are nudged using the Japanese 55-year Reanalysis (Kobayashi et al., 2015) to simulate substantial atmospheric transport. We used the NICAM-TM version described by Niwa et al. (2017) for the transport of CO.

Fossil fuel, biogenic, and biomass burning CO-emission-inventories were used as the CO emission sources at the Earth's surface. The fossil fuel CO emissions were derived from the Emissions Database for Global Atmospheric Research (EDGAR v4.3.2; Janssens-Maenhout et al., 2019) with an annual resolution. Biogenic CO emissions from vegetation were derived from a process-based model, the Vegetation Integrative SImulator for Trace gases (VISIT; Ito, 2019). The biogenic CO emissions in VISIT are simulated as a part of processes associated with biogenic volatile organic compound emissions and have a monthly resolution. For CO emissions from BB, the abovementioned four scenarios based on the various combinations of the LCC and AGB maps.

2.3 Observational data

Ground-based observations of atmospheric CO concentrations were downloaded from the World Data Centre for Greenhouse Gases (WDCGG) for 2009–2015. We used daily data from three ground-based sites: Bukit Kototabang, Indonesia (BKT, 0.20°S, 100.32°E; Zellweger et al., 2019), East Trout Lake, Canada (ETL, 54.35°N, 104.99°W; Kim, 2016), and Minamitorishima, Japan (MNM, 24.29°N, 153.98°E; Watanabe et al., 2000) to evaluate our BB products. The MNM site is situated on a remote coral island in the western North Pacific where the influence of local fire events is usually not significant, whereas the data from the BKT and ETL sites may be influenced by wildfires. The data from the BKT and ETL sites were used to evaluate the estimates of BB emissions from local fire events, and those from MNM were used as spatially representative background information.

125 We also used the column-averaged dry-air concentration of CO (XCO) recorded by the Measurements of Pollution in Troposphere (MOPITT) (Deeter et al., 2003) instrument on NASA's Earth Observing System Terra platform. We analyzed the monthly mean XCO distribution products (L3V95.6.3; Deeter et al., 2014) retrieved from both thermal infrared and near-infrared observations for the period 2013–2015.

2.4 Modified index of agreement and standardized anomaly

130 We used the modified index of agreement (MIA) (Willmott et al., 1985) to compare the observed and simulated atmospheric CO concentrations, as follows:

$$\mathrm{MIA} = 1.0 - \frac{\sum_{i=1}^{N}|x_i - y_i|}{\sum_{i=1}^{N}(|y_i - \overline{x}| + |x_i - \overline{x}|)} \tag{3}$$

where x and y are the observed and simulated CO concentrations (ppm) and $\overline{x}$ is the sample mean of x. The MIA calculates normalized value from 0.0 to 1.0 with higher values indicating better agreement between the observations and the model

135 simulations. Correlation coefficient indicates higher value for agreement of phase variations in the variability, whereas the MIA does for both agreements of phase and amplitude gain variations in the variability.

The observational time series from the BKT and ETL sites were used to classify the 'no fire' or 'fire' months based on the standardized anomaly z:

$$z_i = (x_i - \overline{x})/\sigma_x \tag{4}$$

140 where x is the observed daily CO concentration (ppb) and σ_x is the corresponding sample standard deviation. In this study, fire months were empirically identified as having observed CO concentrations corresponding to $z_i \geq 1.5$.

3 Results

AGB is a source of flammable fuels for BB in our estimate. A comparison of the two AGB datasets used (i.e., GEOCARBON and Globbiomass) and the cumulative probabilities within the range of biomass availability of $0 < \mathrm{AGB} \leq 20$ kg m^{-2} are

145 shown in Fig. 1. The distribution of AGB differs between the two products (Fig. 1a), but there is a relationship between them with a correlation of $r = 0.93$. AGB is most often less than 5 kg m^{-2} in both AGB products. AGB availability of $\leq$ 1, 5, and 10 kg m^{-2} accounts for 43%, 76%, and 94%, respectively, all grids for Globbiomass, and 51%, 83%, and 96%, respectively, for GEOCARBON (Fig. 1b). Figure 1b clearly indicates that the probability distribution of AGB availability for Globbiomass reflects larger values relative to that of GEOCARBON. Overall, Globbiomass indicates approximately $1.35\times$ more AGB than

150 GEOCARBON.

https://doi.org/10.5194/bg-2021-130
Preprint. Discussion started: 10 June 2021

The emission factor (EF) and burning efficiency (BE), which are related to the nature of the flammable materials that comprise the AGB and control the BB emissions (Eqs. 1 and 2), are defined by the LCC. To quantify the differences between the two LCC maps used, we calculated global area totals for three vegetation classes: forest, shrub/savanna/grass, and crop, as defined in the GLC2000 and MCD12Q1 LCCs (Table 2). The LCC data from 2009 were used for MCD12Q1 in this comparison. The forest area in GLC2000 was 55.8×10^6 km^2, 199% more than that in MCD12Q1 (28.0×10^6 km^2); the area of shrub/savanna/grass in GLC200 is 56.4×10^6 km^2, 43% less than MCD12Q1 (98.6×10^6 km^2); that of crop in GLC2000 was 28.2×10^6 km^2, 181% more than MCD12Q1 (15.6×10^6 km^2). At the global scale, it is noteworthy that there are large differences in the area totals of the vegetation classes between the two products; e.g., GLC2000 possesses larger forest areas, whereas MCD12Q1 has more shrub/savanna/grass. Giri et al. (2005) found that the spatial distribution of vegetation in eight LCC classes shows agreement of 59.5% between the GLC2000 and MCD12Q1 products, and the discrepancies between them occur in southern Siberia, the Sahel region, southeastern Brazil, Southern Australia, and on the Tibetan plateau.

We calculated average annual BB CO emissions (g CO m^{-2} yr^{-1}) for 2009–2015 using the GlcGlob, GlcGeoc, McdGlob, and McdGeoc estimates (Fig. 2a). The averaged BB emission map highlights the large spatial variations in CO emissions. Large BB emissions are found in tropical regions over northern and southern tropical Africa, tropical Asia, and Oceania, as well as the southern Amazon, boreal Eurasia, and northern and southeastern regions of North America. The standard deviation among the four BB emissions estimates increases as BB emissions increase, particularly in northern and southern tropical Africa (Fig. 2b).

Global monthly BB CO emissions exhibit seasonal variability with peaks during the boreal summer for all estimates (Fig. 3a). In addition, the GlcGlob and McdGlob estimates show second peaks during the austral summer, whereas the GlcGeoc and McdGeoc estimates show no well-defined peaks. This suggests that the seasonal variability among the BB estimates will change depending on the AGB map, and that the emission totals vary with both the AGB and LCC maps. The annual emission totals vary significantly depending on which BB estimates are used. The mean annual BB emissions with their standard deviation are 526 ± 53, 219 ± 35, 624 ± 57, and 293 ± 44 Tg CO yr^{-1}, for GlcGlob, GlcGeoc, McdGlob, and McdGeoc, respectively. Using data from over 370 publications, Andreae (2019) obtained CO emissions in the range 390–1,210 Tg CO yr^{-1} from open vegetation fires and 181–196 Tg CO yr^{-1} from indoor biofuel use. Our study does not take separate account of emissions from biofuel use, which could result in a slight underestimation of total emissions from BB. The annual CO emissions from BB reported in Andreae (2019) span a wide range, and our emissions estimates based on GlcGlob and McdGlob fall within this range. However, our estimates based on GlcGeoc and McdGeoc fall substantially below this range.

To evaluate the sensitivity of BB emissions estimates to land surface information at the regional scale, we next compared seasonal variability in BB CO emissions from the four estimates over southern tropical Africa (see red rectangle in Fig. 2b) (Fig. 3b). This region is situated in a complicated transition zone containing forest, -savanna, and -bare ground, and with few local studies, and this has led to poor quality land surface information and a high degree of variability among the datasets (Bouvet et al., 2018). All estimates reveal fire emissions from May to October. The annual emissions estimates based on the four AGB/LCC scenarios range over a factor of 4 from 36 to 146 Tg CO yr^{-1} among the estimates. In southern tropical Africa, McdGlob has the highest AGB of 2,704 g m^{-2} for shrub/savanna/grass with higher BE (Table 3), and this rich supply

https://doi.org/10.5194/bg-2021-130
Preprint. Discussion started: 10 June 2021

of flammable fuel leads to the highest CO emissions. For the McdGlob estimate, the AGB of 3.1% for shrub/savanna/grass is burned annually and is converted into emissions. By contrast, GlcGeoc has the lowest AGB for shrub/savanna/grass (28 g m^{-2}) and this results in the lowest CO emissions. The high discrepancy of CO emissions for this area is resulted from the difference of AGBs for forest and shrub/savanna/grass among the four scenarios.

As an alternative approach, we compared each BB estimate in the atmospheric CO field. Variability in atmospheric CO concentrations was simulated using NICAM-TM with surface flux information including the four BB emissions estimates. Observed and simulated daily time series at the three ground-based observation sites, BKT, ETL, and MNM are shown in Fig. 4. The observations at the BKT site in Indonesia are subject to recurrent fire events leading to daily average CO concentrations that exceeded 1000 ppb in 2014 and 2015. For fire months, the mean and standard deviation of the observations reach 660.2 ± 707.5 ppb, whereas those for the no fire months are 153.3 ± 53.2 ppb (Table 4). Regardless of which BB emissions estimate is used, the simulated variability is often closer to the observations for atmospheric concentrations below 200 ppb, which reflects a reduced impact from local fire events, and represents the majority of the observations (Fig. 5). Deviation of the simulated variability from the observations increases with increases in the observed atmospheric concentration above 200 ppb, and this is associated with intermittent fire events. The deviation is especially apparent for simulations based on BB estimates that used the GEOCARBON AGB map, with lower correlation coefficients and MIA than those that used Globbiomass (Table 4). Figures 4 and 5 reveal a difficulty in reproducing the higher CO concentrations generated by sudden BB emissions from intermittent fire events in the simulations, resulting in large absolute errors of 383.4 to 459.5 ppb for fire months.

At the ETL site in Canada, fire months were observed every year except 2009, and atmospheric CO concentrations greater than 1000 ppb were recorded in 2015 (Fig. 4). Almost all of these fire events are represented in the simulations, but the greater deviation from the observations is also apparent at the ETL site for fire months, especially for fire events with atmospheric CO concentrations above 400 ppb (Fig. 5). Although the median values of the simulated concentrations generated using McdGlob are relatively closer to the observations than those based on the other BB estimates under fire events, overestimation when the atmospheric CO concentration was lower than 300 ppb resulted in a worse MIA value (Table 4). At the MNM site in Japan, with no local fire events, there was no clear difference among the BB emissions estimates in terms of the correlation coefficient, mean absolute error, and MIA. Differences in the mean CO concentration among the simulations at the MNM site (11.5 ppb) were smaller than those at BKT (18.8 ppb) and ETL (22.9 ppb) for the no fire months. However, the difference at the MNM site implies that differences in BB emissions estimates can even contribute to variability in the background atmospheric CO concentration, even though CO has a relatively short lifespan in the atmosphere of weeks to months.

To extend the comparison over the regional scale, the global distributions of XCO (ppb) were averaged for 2013–2015, for the MOPITT observations and the simulations using the four BB emissions estimates (Fig. 6). All of the results in Fig. 6 show strong spatial variations in XCO. Higher concentrations of XCO are found over the Tropical regions, southeastern North America, boreal Eurasia, and southeast Asia in the MOPITT observations. These regions are consistent with the areas with large BB emissions, as shown in Fig. 2. Lower XCO concentrations are found over the oceans in the southern hemisphere in the MOPITT observations. These global distributions of XCO are represented in the simulations from all of the BB emissions estimates, but the mean XCO concentrations at the regional scale differ in the simulations among the BB emissions estimates.

https://doi.org/10.5194/bg-2021-130
Preprint. Discussion started: 10 June 2021

Figure 7 shows monthly variations in mean XCO (ppb) and the root mean square error (RMSE, ppb) between the observed and simulated XCO fields over six selected areas: southeastern North America (SEN), Eastern Siberia (ESB), the Amazon (AMZ), South Asia (SAS), Central Africa (CAF), and the Sumatra and Borneo Islands (SBI), which are shown in the red rectangle in Fig. 6a. Over the SEN and ESB areas, the monthly mean observed XCO shows little seasonality, with standard deviations of 10.0 and 9.5 ppb (Fig. 7a and b; Table 5). During the approximately three months of the year with higher XCO concentrations, the mean observed XCO concentrations over both areas increases by approximately 17% relative to the other months. The XCO values simulated using GlcGlob and McdGlob largely reproduce the observed seasonality, but those from GlcGeoc and McdGeoc show less seasonality, resulting in a higher RMSE and lower MIA. Underestimations of both peak concentrations and seasonal variability in simulations with GlcGeoc and McdGeoc are also apparent over the AMZ and SAS areas, with moderate seasonality and standard deviations of 21.1 and 23.5 ppb, respectively, and also over the CAF and SBI areas, with large seasonality and standard deviations of 27.4 and 30.2 ppb, respectively. The XCO values simulated using GlcGlob and McdGlob, on the other hand, successfully recreate the observed variability, such as the abrupt increase in XCO (197.5 ppb) in October 2015 over the SBI area, with monthly mean values of 194.1 and 182.0 ppb, respectively. However, McdGlob overestimates BB emissions during the fire seasons over the CAF relative to the observations. Values of MIA show that the mean value over the six areas was highest in the simulations based on GlcGlob, with a value of 0.64 (0.58 to 0.71), whereas those made using GlcGeoc, McdGlob, and McdGeoc, were 0.49 (0.39 to 0.59), 0.60 (0.54 to 0.71), and 0.53 (0.41 to 0.65), respectively.

4 Discussion

BB emissions are an important contributor to atmospheric greenhouse gases and aerosols, yet uncertainty with respect to regional and interannual variability remains due to our limited understanding of the underlying mechanisms and lack of data related to this variability. Accurate and detailed information regarding AGB and LCC is essential to estimates of BB emissions from wildfires using the bottom-up approach. Improvements in satellite sensors, ground surface observations, digital image processing techniques, and retrieval algorithms have contributed towards reducing the uncertainties associated with AGB and LCC mapping (e.g., Goetz et al., 2009; Clerici et al., 2017). Nevertheless, datasets prepared using different data sources, classification schemes, and methodologies generate discrepancies in the AGB and LCC distributions among the products (Fig. 1; Table 2) as has been discussed previously (e.g., Giri et al., 2005).

This study tested combinations of two sources of AGB data, Globbiomass and GEOCARBON, and two sources of LCC data, GLC2000 and MCD12Q1, and used the same burned area satellite data to estimate BB CO emissions. Although the EF and BE parameters remained the same in our estimates, our analysis showed large discrepancies in annual mean CO emissions, with a factor of approximately 3 (219 – 624 Tg CO yr^{-1}) separating the four BB emissions estimates. Using AGB data from Globbiomass and GEOCARBON, we showed that the magnitude of AGB from Globbiomass tends to be larger than that from GEOCARBON in approximately 35%, leading to the resulting BB emissions estimates based on Globbiomass being more than twice those made using GEOCARBON over the globe. Furthermore, our comparison of the LCC data showed that the global

https://doi.org/10.5194/bg-2021-130
Preprint. Discussion started: 10 June 2021

area totals for the forest class in GLC200 were approximately twice those for MCD12Q1, while those for shrub/savanna/grass in GLC2000 were approximately half those in MCD12Q1. As burning efficiencies for shrub/savanna/grass are greater than those for forests (Table A1 and A2), the BB emissions based on MCD12Q1, with its larger area totals for shrub/savanna/grass, tend to be higher than those based on GLC2000. These results indicate that the estimates of BB emissions are highly sensitive to the AGB and LCC data, and thus the AGB and LCC data used could be the primary drivers of uncertainty in the estimates of BB emissions. In addition, because adequately accurate distributions of AGB and LCC are still unavailable, an independent approach is needed to evaluate the estimate of BB emissions.

Variability in atmospheric CO concentrations simulated using an atmospheric tracer transport model and the BB emissions and other emission inventories were compared with ground-based and satellite observations to act as the independent evaluation of the BB emissions estimates. We did not take account of errors introduced by the observational processes or errors in the transport model and the other emission inventories, but we consider that our analysis is a useful way to study the relative differences among the BB emissions estimates and approximate changes in the simulated atmospheric concentrations. Extending this analysis to ground-based observations of the impact of intermittent fire events at the local scale was more challenging due to the coarse resolution of the available BB emissions estimates and the atmospheric tracer transport model, which weakens temporal and spatial variability in the simulated atmospheric CO concentrations. Abrupt variability in atmospheric CO concentrations recorded in the ground-based observations for fire months were indeed represented with the variations that are attenuated in the higher CO concentrations (Fig. 4). Relatively small differences among the BB emissions estimates from the ground-based observation sites (Table 4) may be attributed to the loss of information related to the high-frequency variability in the simulated atmospheric CO concentration. We need to recognize that a global transport model with a horizontal resolution of about 220 km is insufficient to quantify local BB emissions accurately. The attenuation in the simulation can be moderately improved by including daily variability in the BB emissions, especially for surface observations with high levels of biomass burning, using atmospheric transport simulations with a high spatial resolution (e.g., Mu et al., 2011).

At the global scale, comparison with the satellite observations suggested that the XCO variability simulated using the AGB data from Globbiomass, especially the GlcGlob estimate, which was compiled using the LCC data from GLC2000, provided a better representation of the temporal and spatial variability in the observed XCO during both the no fire and fire seasons, relative to those based on the AGB data from GEOCARBON (Figs 6 and 7; Table 5). The GlcGlob estimate yields global BB emissions of 526 ± 53 Tg CO yr^{-1}. These total CO emissions are slightly higher than those reported by Hooghiemstra et al. (2011), who found total emissions of 400 ± 88 and 482 ± 68 Tg CO yr^{-1} for 2003 and 2004, respectively, using a data assimilation to surface observations. The corresponding mean emissions for 1997 and 2016 obtained from bottom-up estimates by van der Werf et al. (2017) were 357 Tg CO yr^{-1}, which is approximately 32% lower than GlcGlob.

Note that our analysis is not a guarantee of the validity of the AGB and LCC data used, and we do not intend to argue which of the AGB and LCC datasets are better than others. As CO EFs remain uncertain, due mainly to the difficulty in treatment of emissions from residual smoldering combustion (Andreae, 2019), the estimated BB emissions can vary according to the EF used and depend on the selection of the fire class confidence in the fire mask data. Additionally, one limitation of the current study of BB estimates is that it does not include a scheme to inherit the amount of AGB that remained unburned in the previous year. Although continuous variations in AGB over multiyear periods, and the impact of these variations on BB emissions, can be simulated by coupling the system to a terrestrial biosphere model, this work remains incomplete. Finally, to improve our currently limited ability to estimate BB emissions, we are calling for additional independent approaches and data evaluation to help increase our understanding of their characteristics.

5 Conclusions

This study used the burned area method in bottom-up approaches to estimate spatiotemporal variations in global BB CO emissions based on AGB and LCC land surface information and burned area data. Regarding the land surface information, we tested two AGB datasets (Globbiomass and GEOCARBON) to evaluate the sensitivity of BB emissions estimates to these different datasets. Preliminary comparisons of the AGB and LCC datasets showed substantial differences among them. The spatial distribution of AGB was highly correlated between Globbiomass and GEOCARBON, but the former contained AGB values that were larger than the latter by a factor of 1.35. The global area total for forest in GLC2000 was 199% more than that in MCD12Q1, but was 43% less than for shrub/savanna/grass. By combining these AGB and LCC data with the burned area data, four BB emissions estimates (i.e., GlcGlob, GlcGeoc, McdGlob, and McdGeoc) were derived using the burned area method.

We began by comparing the seasonal variability of the BB emissions estimates over the regional and global scales. This comparison showed that BB emissions increase as the amount of AGB for shrub/savanna/grass increases over the corresponding burned area. Our estimates of the mean annual BB emissions resulted in a large divergence among the estimates; i.e., 526 ± 53, 219 ± 35, 624 ± 57, and 293 ± 44 Tg CO yr^{-1} for GlcGlob, GlcGeoc, McdGlob, and McdGeoc, respectively. Using the BB emissions estimates, variability in atmospheric CO concentrations was simulated using NICAM-TM with other emissions sources (i.e., fossil fuel and biogenic emissions) as inputs. We evaluated our results against independent ground-based (WDCGG network) and satellite (MOPITT) CO observations. Comparison with data from the ground-based sites indicated that all BB emissions estimates represent local fire events, but underestimation of BB emissions was particularly apparent for intense fires at the BKT site in Indonesia. Explicit differences in the simulated CO concentrations among the BB emissions estimates were found in comparison with the satellite observations at the regional scale. In our simulations, the XCO variability simulated using the GlcGlob estimates was the most consistent with the satellite observations at the regional and global scales.

This study has confirmed that BB emissions estimates are sensitive to the land surface information on which they are based. Furthermore, although it is clear that there are significant differences among the various land surface information products currently available, the quantitative evaluation of these differences remains difficult because of the limited coverage of surface observations. One approach to addressing this limitation would be the commissioning of future satellite missions carrying higher-resolution onboard sensors.

https://doi.org/10.5194/bg-2021-130
Preprint. Discussion started: 10 June 2021

Biogeosciences Discussions

Acknowledgements. This study was supported by the GOSAT-2 project at the National Institute for Environmental Studies (NIES) and the Climate Change Adaptation Research Program of NIES. The simulations were completed using the supercomputer (NEC SX-Aurora TSUBASA) at NIES. We thank the EDGAR, ESA, GEOCARBON, GLC2000, Globbiomass, JRA-55, MODIS, MOPITT, and WDCGG teams, as well as Dr. Akihiko Ito (NIES), for providing the data used in this study. BKT is operated by the Indonesian Agency for Meteorology Climatology and Geophysics (BMKG) with support from the WMO/GAW Quality Assurance/Science Activity Centre Switzerland (QA/SAC-CH).

https://doi.org/10.5194/bg-2021-130
Preprint. Discussion started: 10 June 2021

References

Akagi, S., Yokelson, R. J., Wiedinmyer, C., Alvarado, M., Reid, J., Karl, T., Crounse, J., and Wennberg, P.: Emission factors for open and domestic biomass burning for use in atmospheric models, Atmospheric Chemistry and Physics, 11, 4039–4072, 2011.

Andreae, M. O.: Biomass burning: its history, use, and distribution and its impact on environmental quality and global climate, in: Global biomass burning: Atmospheric, climatic and biospheric implications, edited by Levine, J. S., pp. 3–21, MIT Press, Cambridge, Mass, 1991.

Andreae, M. O.: Emission of trace gases and aerosols from biomass burning–an updated assessment, Atmospheric Chemistry and Physics, 19, 8523–8546, 2019.

Andreae, M. O. and Merlet, P.: Emission of trace gases and aerosols from biomass burning, Global biogeochemical cycles, 15, 955–966, 2001.

Avitabile, V., Herold, M., Heuvelink, G. B., Lewis, S. L., Phillips, O. L., Asner, G. P., Armston, J., Ashton, P. S., Banin, L., Bayol, N., et al.: An integrated pan-tropical biomass map using multiple reference datasets, Global change biology, 22, 1406–1420, 2016.

Baccini, A., Goetz, S., Walker, W., Laporte, N., Sun, M., Sulla-Menashe, D., Hackler, J., Beck, P., Dubayah, R., Friedl, M., et al.: Estimated carbon dioxide emissions from tropical deforestation improved by carbon-density maps, Nature climate change, 2, 182–185, 2012.

Balch, J. K., Bradley, B. A., Abatzoglou, J. T., Nagy, R. C., Fusco, E. J., and Mahood, A. L.: Human-started wildfires expand the fire niche across the United States, Proceedings of the National Academy of Sciences, 114, 2946–2951, 2017.

Bartholomé, E. and Belward, A. S.: GLC2000: a new approach to global land cover mapping from Earth observation data, International Journal of Remote Sensing, 26, 1959–1977, 2005.

Bougiatioti, A., Stavroulas, I., Kostenidou, E., Zarmpas, P., Theodosi, C., Kouvarakis, G., Canonaco, F., Prévôt, A. S., Nenes, A., Pandis, S. N., et al.: Processing of biomass-burning aerosol in the eastern Mediterranean during summertime, Atmospheric Chemistry and Physics, 14, 4793–4807, 2014.

Bouvet, A., Mermoz, S., Le Toan, T., Villard, L., Mathieu, R., Naidoo, L., and Asner, G. P.: An above-ground biomass map of African savannahs and woodlands at 25 m resolution derived from ALOS PALSAR, Remote sensing of environment, 206, 156–173, 2018.

Chen, Y., Li, Q., Randerson, J., Lyons, E., Kahn, R., Nelson, D., and Diner, D.: The sensitivity of CO and aerosol transport to the temporal and vertical distribution of North American boreal fire emissions, Atmospheric Chemistry and Physics, 9, 6559–6580, 2009.

Clerici, N., Valbuena Calderón, C. A., and Posada, J. M.: Fusion of Sentinel-1A and Sentinel-2A data for land cover mapping: a case study in the lower Magdalena region, Colombia, Journal of Maps, 13, 718–726, 2017.

Deeter, M., Martínez-Alonso, S., Edwards, D., Emmons, L., Gille, J., Worden, H., Sweeney, C., Pittman, J., Daube, B., and Wofsy, S.: The MOPITT Version 6 product: algorithm enhancements and validation, Atmospheric Measurement Techniques, 7, 3623, 2014.

Deeter, M. N., Emmons, L. K., Francis, G. L., Edwards, D. P., Gille, J. C., Warner, J. X., Khattatov, B., Ziskin, D., Lamarque, J. F., Ho, S. P., Yudin, V., Attié, J. L., Packman, D., Chen, J., Mao, D., and Drummond, J. R.: Operational carbon monoxide retrieval algorithm and selected results for the MOPITT instrument, Journal of Geophysical Research, 108, 4399, 2003.

Dutta, R., Das, A., and Aryal, J.: Big data integration shows Australian bush-fire frequency is increasing significantly, Royal Society open science, 3, 150 241, 2016.

Giglio, L., van der Werf, G., Randerson, J., Collatz, G., and Kasibhatla, P.: Global estimation of burned area using MODIS active fire observations., Atmospheric Chemistry and Physics, 6, 957–974, 2006.

https://doi.org/10.5194/bg-2021-130
Preprint. Discussion started: 10 June 2021

Giglio, L., Schroeder, W., and Justice, C. O.: The collection 6 MODIS active fire detection algorithm and fire products, Remote Sensing of Environment, 178, 31–41, 2016.

Giri, C., Zhu, Z., and Reed, B.: A comparative analysis of the Global Land Cover 2000 and MODIS land cover data sets, Remote sensing of environment, 94, 123–132, 2005.

Goetz, S. J., Baccini, A., Laporte, N. T., Johns, T., Walker, W., Kellndorfer, J., Houghton, R. A., and Sun, M.: Mapping and monitoring carbon stocks with satellite observations: a comparison of methods, Carbon balance and management, 4, 2, 2009.

Hart, S. J., Henkelman, J., McLoughlin, P. D., Nielsen, S. E., Truchon-Savard, A., and Johnstone, J. F.: Examining forest resilience to changing fire frequency in a fire-prone region of boreal forest, Global change biology, 25, 869–884, 2019.

Hooghiemstra, P., Krol, M., Meirink, J., Bergamaschi, P., Van Der Werf, G., Novelli, P., Aben, I., and Röckmann, T.: Optimizing global CO emission estimates using a four-dimensional variational data assimilation system and surface network observations, Atmospheric chemistry and physics, 11, 4705–4723, 2011.

Ito, A.: Disequilibrium of terrestrial ecosystem CO_2 budget caused by disturbance-induced emissions and non-CO_2 carbon export flows: a global model assessment, Earth System Dynamics, 10, 685–709, 2019.

Janssens-Maenhout, G., Crippa, M., Guizzardi, D., Muntean, M., Schaaf, E., Dentener, F., Bergamaschi, P., Pagliari, V., Olivier, J. G., Peters, J. A., et al.: EDGAR v4. 3.2 Global Atlas of the three major greenhouse gas emissions for the period 1970–2012, Earth System Science Data, 11, 959–1002, 2019.

Kaiser, J., Heil, A., Andreae, M., Benedetti, A., Chubarova, N., Jones, L., Morcrette, J.-J., Razinger, M., Schultz, M., Suttie, M., et al.: Biomass burning emissions estimated with a global fire assimilation system based on observed fire radiative power, Biogeosciences, 9, 527, 2012.

Kim, M.: Variations and Sources of Atmospheric CO_2 Measured at East Trout Lake, Canada, Ph.D. thesis, University of Waterloo, 2016.

Kobayashi, S., Ota, Y., Harada, Y., Ebita, A., Moriya, M., Onoda, H., Onogi, K., Kamahori, H., Kobayashi, C., Endo, H., et al.: The JRA-55 reanalysis: General specifications and basic characteristics, Journal of the Meteorological Society of Japan. Ser. II, 93, 5–48, 2015.

Michel, C., Liousse, C., Grégoire, J.-M., Tansey, K., Carmichael, G., and Woo, J.-H.: Biomass burning emission inventory from burnt area data given by the SPOT-VEGETATION system in the frame of TRACE-P and ACE-Asia campaigns, Journal of Geophysical Research: Atmospheres, 110, 2005.

Mieville, A., Granier, C., Liousse, C., Guillaume, B., Mouillot, F., Lamarque, J., Grégoire, J., and Pétron, G.: Emissions of gases and particles from biomass burning during the 20th century using satellite data and an historical reconstruction, Atmospheric Environment, 44, 1469–1477, 2010.

Mitchard, E. T., Saatchi, S. S., Baccini, A., Asner, G. P., Goetz, S. J., Harris, N. L., and Brown, S.: Uncertainty in the spatial distribution of tropical forest biomass: a comparison of pan-tropical maps, Carbon Balance and Management, 8, 10, 2013.

Mu, M., Randerson, J., Van der Werf, G., Giglio, L., Kasibhatla, P., Morton, D., Collatz, G., DeFries, R., Hyer, E., Prins, E., et al.: Daily and 3-hourly variability in global fire emissions and consequences for atmospheric model predictions of carbon monoxide, Journal of Geophysical Research: Atmospheres, 116, 2011.

Niwa, Y., Patra, P., Sawa, Y., Machida, T., Matsueda, H., Belikov, D., Maki, T., Ikegami, M., Imasu, R., Maksyutov, S., et al.: Three-dimensional variations of atmospheric CO_2: aircraft measurements and multi-transport model simulations, Atmospheric Chemistry and Physics, 11, 13 359–13 375, 2011.

Niwa, Y., Tomita, H., Satoh, M., Imasu, R., Sawa, Y., Tsuboi, K., Matsueda, H., Machida, T., Sasakawa, M., Belan, B., et al.: A 4D-Var inversion system based on the icosahedral grid model (NICAM-TM 4D-Var v1. 0)–Part 1: Offline forward and adjoint transport models, Geoscientific Model Development, 10, 1157–1174, 2017.

Niwa, Y., Sawa, Y., Nara, H., Machida, T., Matsueda, H., Umezawa, T., Ito, A., Nakaoka, S.-I., Tanimoto, H., and Tohjima, Y.: Estimation of fire-induced carbon emission from Equatorial Asia in 2015 by using in situ aircraft and ship observations, Atmospheric Chemistry and Physics Discussions, 2020, 1–31, 2020.

Pan, X., Ichoku, C., Chin, M., Bian, H., Darmenov, A., Colarco, P., Ellison, L., Kucsera, T., da Silva, A., Wang, J., et al.: Six global biomass burning emission datasets: intercomparison and application in one global aerosol model, Atmospheric Chemistry and Physics, 20, 969–994, 2020.

Patra, P. K., Houweling, S., Krol, M., Bousquet, P., Belikov, D., Bergmann, D., Bian, H., Cameron-Smith, P., Chipperfield, M. P., Corbin, K., Fortems-Cheiney, A., Fraser, A., Gloor, E., Hess, P., Ito, A., Kawa, S. R., Law, R. M., Loh, Z., Maksyutov, S., Meng, L., Palmer, P. I., Prinn, R. G., Rigby, M., Saito, R., and Wilson, C.: TransCom model simulations of CH_4 and related species: linking transport, surface flux and chemical loss with CH_4 variability in the troposphere and lower stratosphere, Atmospheric Chemistry and Physics, 11, 12 813–12 837, 2011.

Popescu, S. C., Zhao, K., Neuenschwander, A., and Lin, C.: Satellite lidar vs. small footprint airborne lidar: Comparing the accuracy of aboveground biomass estimates and forest structure metrics at footprint level, Remote Sensing of Environment, 115, 2786–2797, 2011.

Rodriguez-Galiano, V. F., Ghimire, B., Rogan, J., Chica-Olmo, M., and Rigol-Sanchez, J. P.: An assessment of the effectiveness of a random forest classifier for land-cover classification, ISPRS Journal of Photogrammetry and Remote Sensing, 67, 93–104, 2012.

Saatchi, S. S., Harris, N. L., Brown, S., Lefsky, M., Mitchard, E. T. A., Salas, W., Zutta, B. R., Buermann, W., Lewis, S. L., Hagen, S., Petrova, S., White, L., Silman, M., and Morel, A.: Benchmark map of forest carbon stocks in tropical regions across three continents, Proceedings of the National Academy of Science of the United States of America, 108, 9899–9904, 2011.

Saito, M., Luyssaert, S., Poulter, B., Williams, M., Ciais, P., Bellassen, V., Ryan, C. M., Yue, C., Cadule, P., and Peylin, P.: Fire regimes and variability in aboveground woody biomass in miombo woodland, Journal of Geophysical Research: Biogeosciences, 119, 1014–1029, 2014.

Santoro, M.: GlobBiomass - global datasets of forest biomass, https://doi.org/10.1594/PANGAEA.894711, https://doi.org/10.1594/PANGAEA.894711, 2018.

Satoh, M.: Conservative scheme for the compressible nonhydrostatic models with the horizontally explicit and vertically implicit time integration scheme, Monthly Weather Review, 130, 1227–1245, 2002.

Seiler, W. and Crutzen, P. J.: Estimates of gross and net fluxes of carbon between the biosphere and the atmosphere from biomass burning, Climatic Change, 2, 207–247, 1980.

Shi, Y., Matsunaga, T., Saito, M., Yamaguchi, Y., and Chen, X.: Comparison of global inventories of CO_2 emissions from biomass burning during 2002–2011 derived from multiple satellite products, Environmental Pollution, 206, 479 – 487, 2015.

Shiraishi, T., Hirata, R., and Hirano, T.: New inventories of global carbon dioxide emissions through biomass burning in 2001–2018, Remore Sensing, 13, 1914, 2021.

Sulla-Menashe, D., Gray, J. M., Abercrombie, S. P., and Friedl, M. A.: Hierarchical mapping of annual global land cover 2001 to present: The MODIS Collection 6 Land Cover product, Remote Sensing of Environment, 222, 183–194, 2019.

Turetsky, M. R., Benscoter, B., Page, S., Rein, G., Van Der Werf, G. R., and Watts, A.: Global vulnerability of peatlands to fire and carbon loss, Nature Geoscience, 8, 11–14, 2015.

https://doi.org/10.5194/bg-2021-130
Preprint. Discussion started: 10 June 2021

van der Werf, G. R., Randerson, J. T., Giglio, L., Van Leeuwen, T. T., Chen, Y., Rogers, B. M., Mu, M., Van Marle, M. J., Morton, D. C., Collatz, G. J., et al.: Global fire emissions estimates during 1997-2016, Earth System Science Data, 9, 697–720, 2017.

Watanabe, F., Uchino, O., Joo, Y., Aono, M., Higashijima, K., Hirano, Y., Tsuboi, K., and Suda, K.: Interannual variation of growth rate of atmospheric carbon dioxide concentration observed at the JMA's three monitoring stations: Large increase in concentration of atmospheric carbon dioxide in 1998, Journal of the Meteorological Society of Japan. Ser. II, 78, 673–682, 2000.

Wiedinmyer, C., Akagi, S., Yokelson, R. J., Emmons, L., Al-Saadi, J., Orlando, J., and Soja, A.: The Fire INventory from NCAR (FINN): A high resolution global model to estimate the emissions from open burning, Geoscientific Model Development, 4, 625, 2011.

Willmott, C. J., Ackleson, S. G., Davis, R. E., Feddema, J. J., Klink, K. M., Legates, D. R., O'donnell, J., and Rowe, C. M.: Statistics for the evaluation and comparison of models, Journal of Geophysical Research: Oceans, 90, 8995–9005, 1985.

Zellweger, C., Steinbacher, M., and Buchmann, B.: System and performance audit of surface ozone, carbon monoxide, methane, and carbon dioxide at the Global GAW Station Bukit Kototabang, Indonesia, WCC-Empa Report 19/1, https://www.empa.ch/web/s503/wcc-empa, 2019.

https://doi.org/10.5194/bg-2021-130
Preprint. Discussion started: 10 June 2021

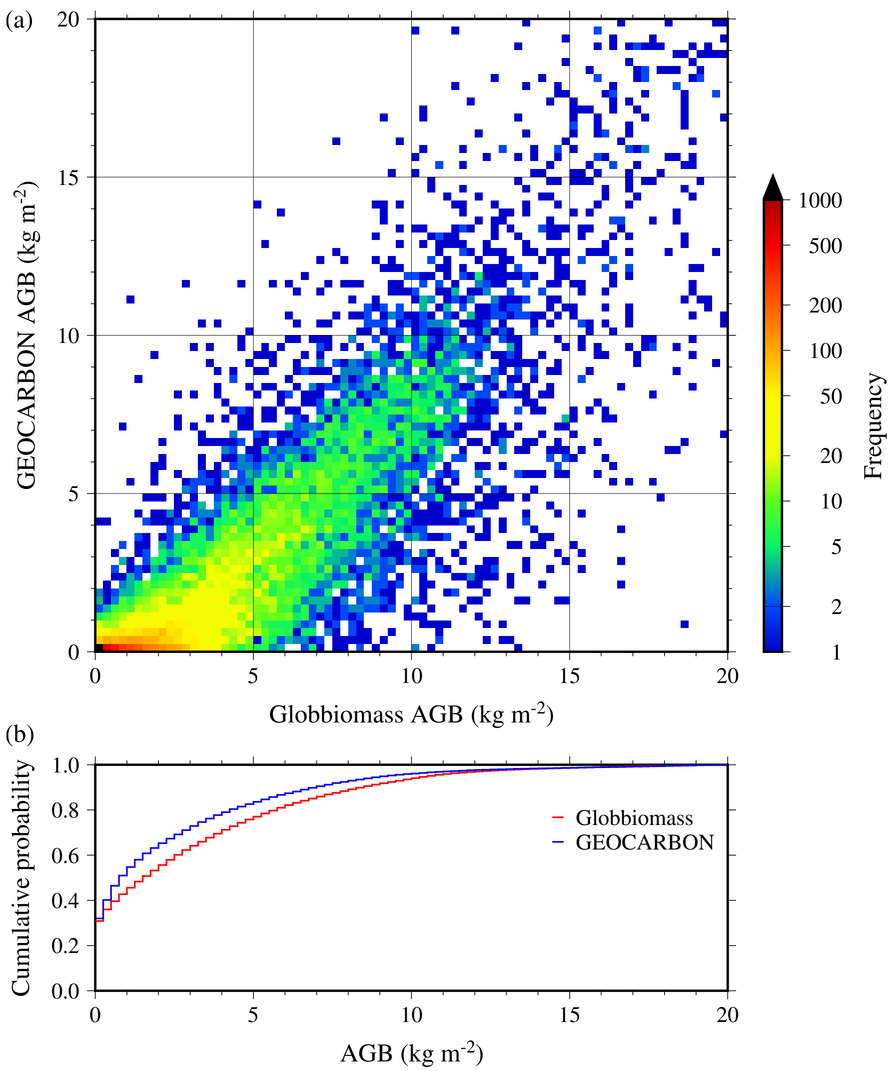

Figure 1. Comparisons of (a) AGB for 2009 based on Globbiomass and GEOCARBON and (b) their histograms.

https://doi.org/10.5194/bg-2021-130
Preprint. Discussion started: 10 June 2021

Biogeosciences
Discussions

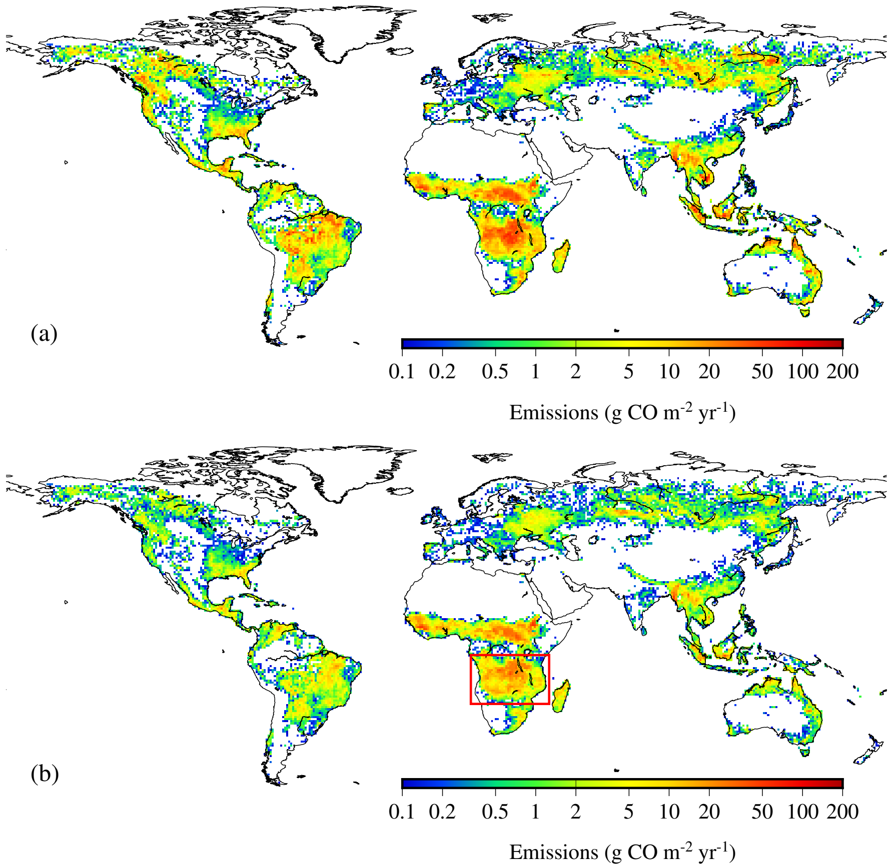

Figure 2. Spatial distributions of (a) the average annual CO emissions (g CO m^{-2} yr^{-1}) and (b) their standard deviation based on four BB emissions estimates (i.e., GlcGlob, GlcGeoc, McdGlob, and McdGeoc) over the period 2009–2015.

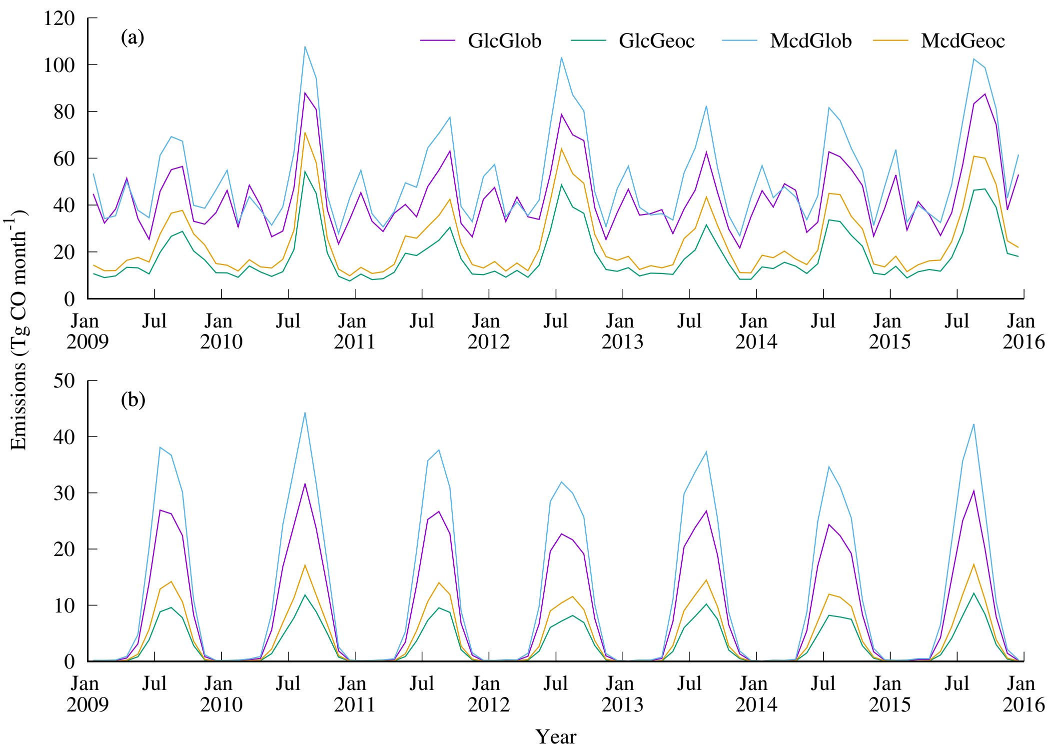

Figure 3. Monthly CO emissions (Tg CO month^{-1}) for GlcGlob (purple line), GlcGeoc (green line), McdGlob (blue line), and McdGeoc (orange line) over (a) the globe and (b) the Southern Africa region within the red rectangle shown in Fig. 2b.

https://doi.org/10.5194/bg-2021-130
Preprint. Discussion started: 10 June 2021

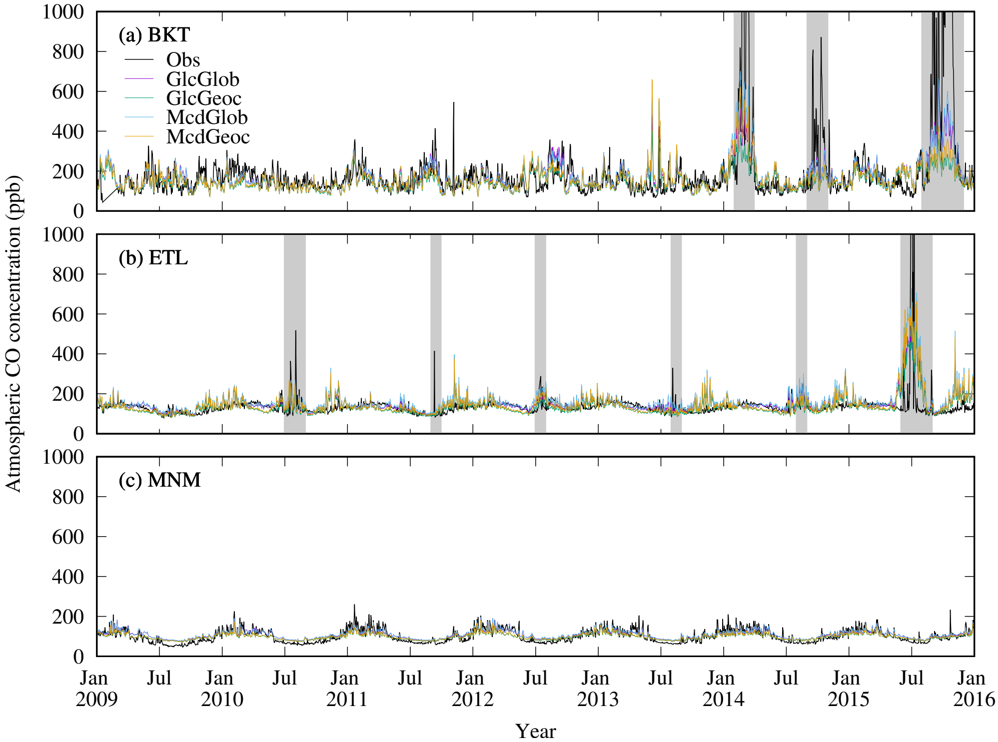

Figure 4. Daily atmospheric CO concentration variations (ppb) at the three ground-based observation stations, (a) Bukit Kototabang (BKT), (b) East Trout Lake (ETL), and (c) Minamitorishima (MNM) for 2009–2015. The grey shading for the BKT and ETL sites indicates the fire months identified using the standardized anomaly (Equation 4).

https://doi.org/10.5194/bg-2021-130
Preprint. Discussion started: 10 June 2021

Biogeosciences
Discussions

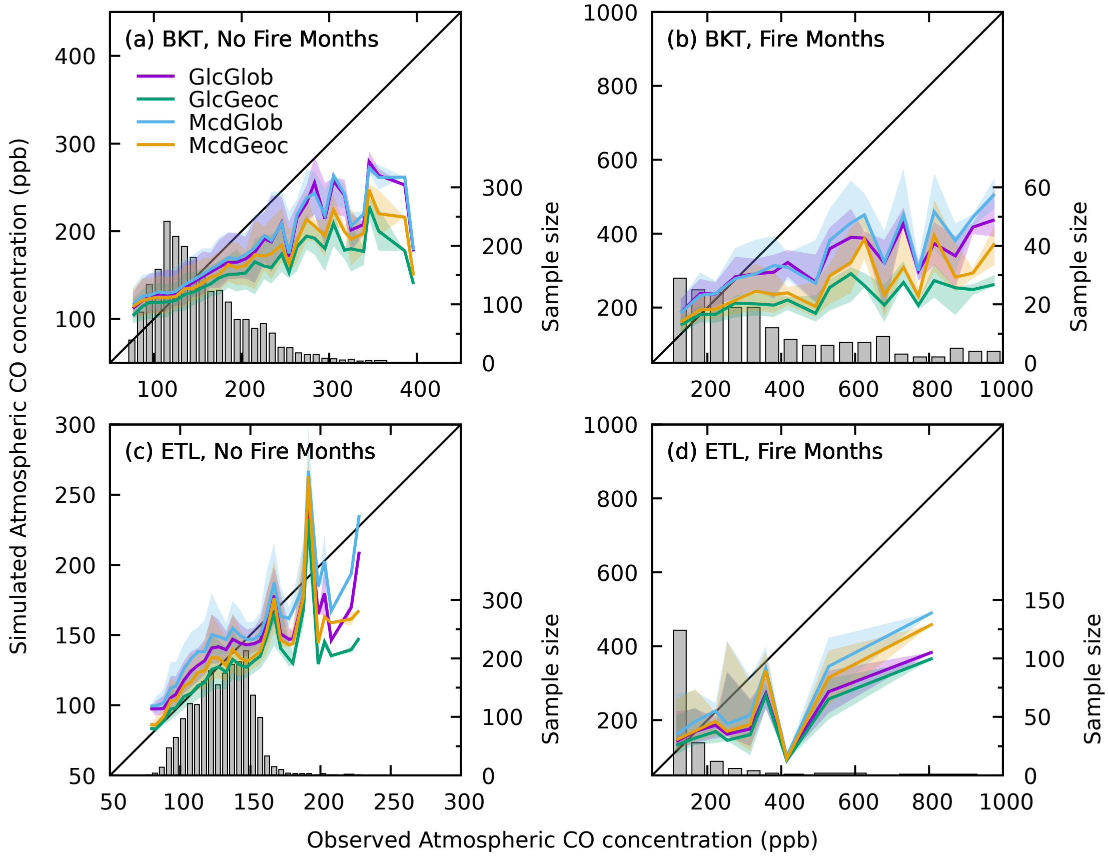

Figure 5. Conditional quantile plots for observed and simulated atmospheric CO concentration (ppb) for both no fire and fire months at (a and b) BKT and (c and d) ETL over the period 2009–2015. Solid lines and shading show median and 0.25th and 0.75th quantiles. Bars in grey are histograms of the observed atmospheric CO concentrations.

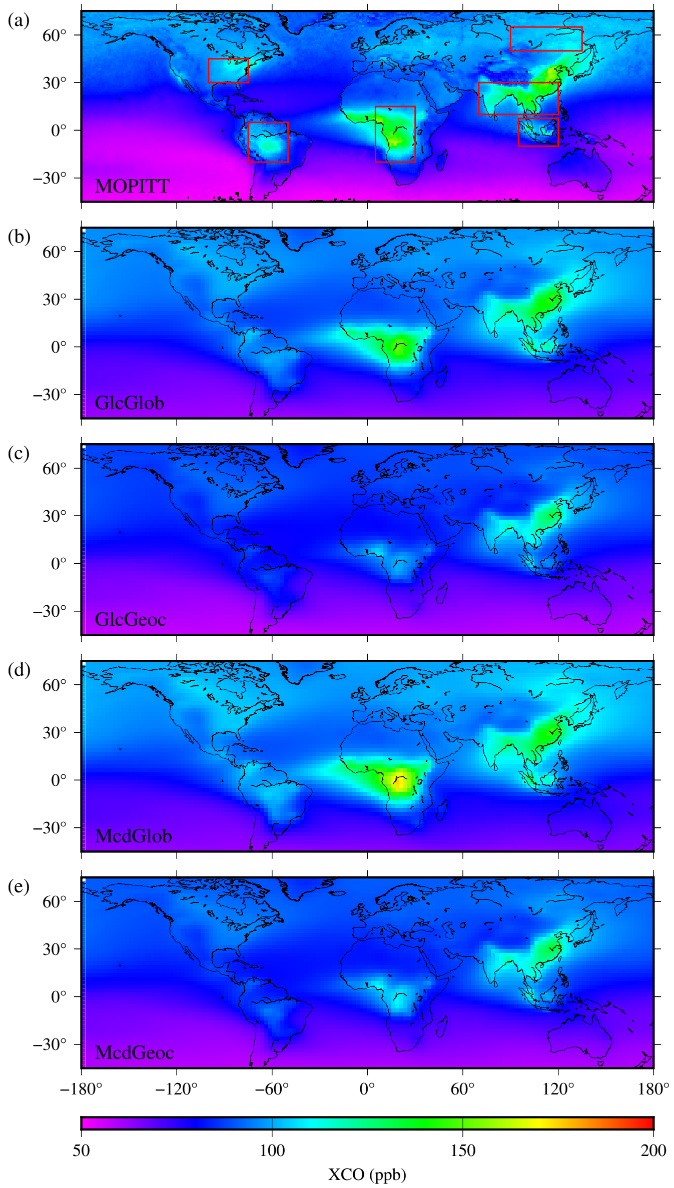

Figure 6. Spatial distributions of mean XCO (ppb) between 2013 and 2015 for (a) MOPITT Level 3 product and the simulations using (b) GlcGlob, (c) GlcGeoc, (d) McdGlob, and (e) McdGeoc.

https://doi.org/10.5194/bg-2021-130
Preprint. Discussion started: 10 June 2021

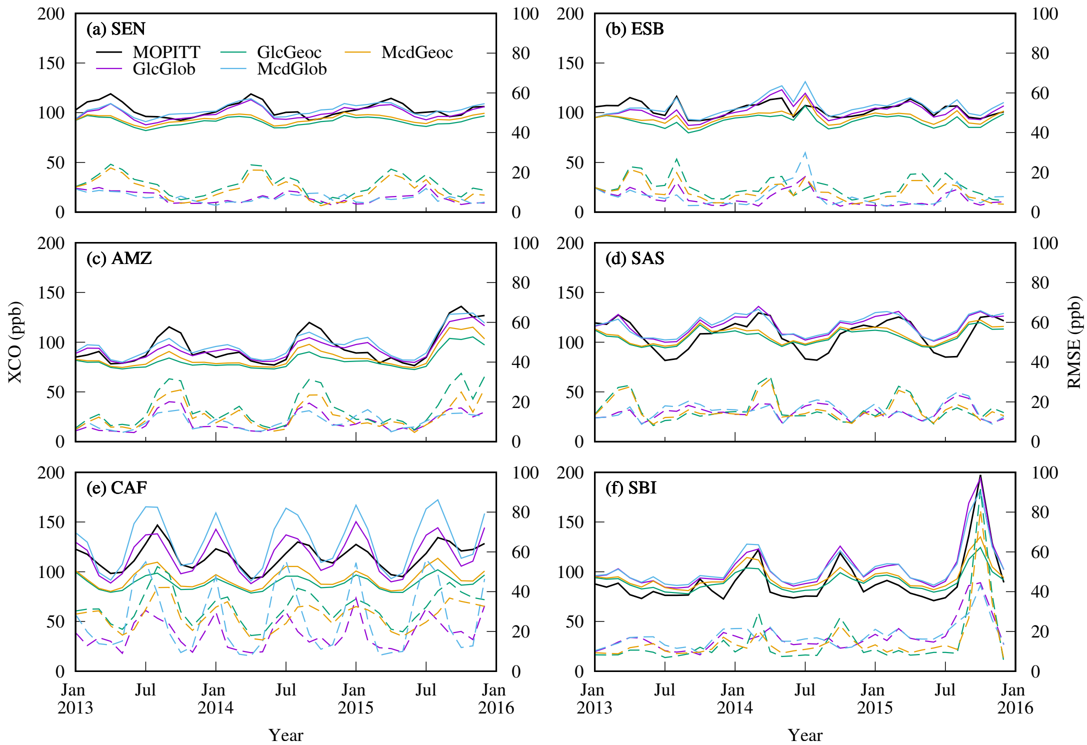

Figure 7. Monthly mean XCO variations (ppb; solid) and RMSE (ppb; dashed) between observed and simulated fields over the six areas: (a) SEN, (b) ESB, (c) AMZ, (d) SAS, (e) CAF, and (f) SBI for 2013–2015.

https://doi.org/10.5194/bg-2021-130
Preprint. Discussion started: 10 June 2021

Table 1. BB emissions estimates and the LCC and AGB data used.

Product	LCC map	AGB map
GlcGlob	GLC2000	Globbiomasss
GlcGeoc	GLC2000	GEOCARBON
McdGlob	MCD12Q1	Globbiomass
McdGeoc	MCD12Q1	GEOCARBON

Table 2. Global area totals (10^6 km^2) for forest, shrub/savanna/grass, and crop land[1] in GLC2000 and MCD12Q1.

Type	GLC2000	MCD12Q1
Forest	55.8	28.0
Shrub/Savanna/Grass	56.4	98.6
Crop	28.2	15.6

[1] Forest: Tree Cover, broadleaved, evergreen, Tree Cover, broadleaved, deciduous, closed and open, Tree Cover, needle-leaved, evergreen and deciduous, Tree Cover, mixed leaf type, and Mosaic: Tree Cover, Other natural vegetation for GLC2000; Evergreen Needleleaf Forest, Evergreen Broadleaf Forest, Deciduous Needleleaf Forest, Deciduous Broadleaf Forests, and Mixed Forests for MCD12Q1. Shrub/Savanna/Grass: Shrub Cover, closed-open, evergreen and deciduous, Herbaceous Cover, closed-open, and Sparse herbaceous or sparse shrub cover for GLC2000; Closed Shrublands, Open Shrublands, Woody Savannas, savannas, and Grassland for MCD12Q1. Crop: Cultivated and managed areas, Mosaic: Cropland, Tree Cover, Other natural vegetation, and Mosaic: Cropland, Shrub and/or grass cover for GLC2000; Croplands and Cropland/Natural Vegetation Mosaics for MCD12Q1.

https://doi.org/10.5194/bg-2021-130
Preprint. Discussion started: 10 June 2021

Table 3. Mean AGB (g m^{-2}) from the four BB emissions estimates for forest and shrub/savanna/grass over southern tropical Africa (Fig. 2b). Numbers in parentheses are the annual AGB decrement (%) caused by fires.

Type	GlcGlob	GlcGeoc	McdGlob	McdGeoc
Forest	3,567 (1.0)	2,749 (0.9)	1,896 (0.7)	1,925 (0.7)
Shrub/Savanna/Grass	738 (2.2)	28 (1.3)	2,704 (3.1)	893 (3.2)

https://doi.org/10.5194/bg-2021-130
Preprint. Discussion started: 10 June 2021

Table 4. Statistics comparing observed and simulated time series of daily atmospheric CO concentrations at the BKT, ETL, and MNM sites between 2009 and 2015.

Statistics	No Fire Months			Fire Months	
	BKT	ETL	MNM	BKT	ETL
No. of Observations	2,236	2,053	2,511	237	226
Mean (ppb)					
Observations	153.3	130.6	101.3	660.2	163.7
GlcGlob	156.3	144.2	107.5	309.4	188.0
GlcGeoc	141.2	130.2	98.1	216.2	175.1
McdGlob	160.0	153.1	109.6	335.9	223.2
McdGeoc	151.0	138.3	100.3	266.0	205.5
Standard deviation (ppb)					
Observations	53.2	19.7	32.1	707.5	196.4
GlcGlob	48.9	29.7	19.8	105.2	107.7
GlcGeoc	39.4	29.3	15.9	57.2	106.3
McdGlob	52.3	34.8	20.0	134.6	144.1
McdGeoc	49.4	34.3	16.5	105.3	139.5
Mean absolute error (ppb)					
GlcGlob	37.6	20.6	15.6	396.4	88.7
GlcGeoc	38.0	20.7	15.6	459.5	84.7
McdGlob	38.8	26.8	16.1	383.4	111.5
McdGeoc	39.4	23.3	15.4	426.6	102.0
Correlation coefficient					
GlcGlob	0.48	0.41	0.87	0.55	0.33
GlcGeoc	0.42	0.38	0.87	0.41	0.33
McdGlob	0.45	0.33	0.88	0.55	0.33
McdGeoc	0.38	0.32	0.87	0.41	0.33
Modified index of agreement					
GlcGlob	0.52	0.46	0.64	0.54	0.41
GlcGeoc	0.49	0.45	0.61	0.51	0.45
McdGlob	0.51	0.39	0.63	0.54	0.35
McdGeoc	0.49	0.41	0.62	0.52	0.40

https://doi.org/10.5194/bg-2021-130
Preprint. Discussion started: 10 June 2021

Biogeosciences Discussions
Open Access

Table 5. As Table 4, but observed and simulated XCO (ppb) fields over the six selected areas: SEN, ESB, AMZ, SAS, CAF, and SBI between 2013 and 2015.

Statistics		SEN	ESB	AMZ	SAS	CAF	SBI
Mean (ppb)							
	MOPITT	103.4	103.1	96.4	110.0	114.6	91.5
	GlcGlob	99.6	101.4	93.8	116.6	116.7	103.4
	GlcGeoc	91.0	91.5	81.7	105.4	88.5	90.4
	McdGlob	102.7	105.8	97.6	117.4	129.8	103.8
	McdGeoc	93.6	95.0	85.7	107.4	93.1	94.1
Standard deviation (ppb)							
	MOPITT	10.0	9.5	21.1	23.5	27.4	30.2
	GlcGlob	6.5	10.3	15.8	19.1	31.3	27.1
	GlcGeoc	4.6	7.7	11.7	14.3	12.9	13.4
	McdGlob	6.3	11.8	17.1	17.6	41.3	24.1
	McdGeoc	4.6	8.9	14.8	14.7	15.9	15.4
Mean absolute error (ppb)							
	GlcGlob	6.0	5.9	8.3	12.5	14.6	15.3
	GlcGeoc	12.6	12.2	15.0	13.4	26.6	12.1
	McdGlob	6.1	6.6	8.4	13.1	20.6	16.0
	McdGeoc	10.3	9.5	11.5	13.1	23.0	12.6
Correlation coefficient							
	GlcGlob	0.73	0.69	0.86	0.82	0.77	0.87
	GlcGeoc	0.63	0.63	0.88	0.71	0.73	0.81
	McdGlob	0.65	0.65	0.86	0.81	0.77	0.89
	McdGeoc	0.60	0.61	0.89	0.71	0.75	0.84
Modified index of agreement							
	GlcGlob	0.58	0.63	0.71	0.62	0.69	0.58
	GlcGeoc	0.39	0.40	0.56	0.57	0.45	0.59
	McdGlob	0.54	0.58	0.71	0.60	0.62	0.55
	McdGeoc	0.42	0.47	0.65	0.57	0.50	0.58

https://doi.org/10.5194/bg-2021-130
Preprint. Discussion started: 10 June 2021

Biogeosciences
Discussions
Open Access
EGU

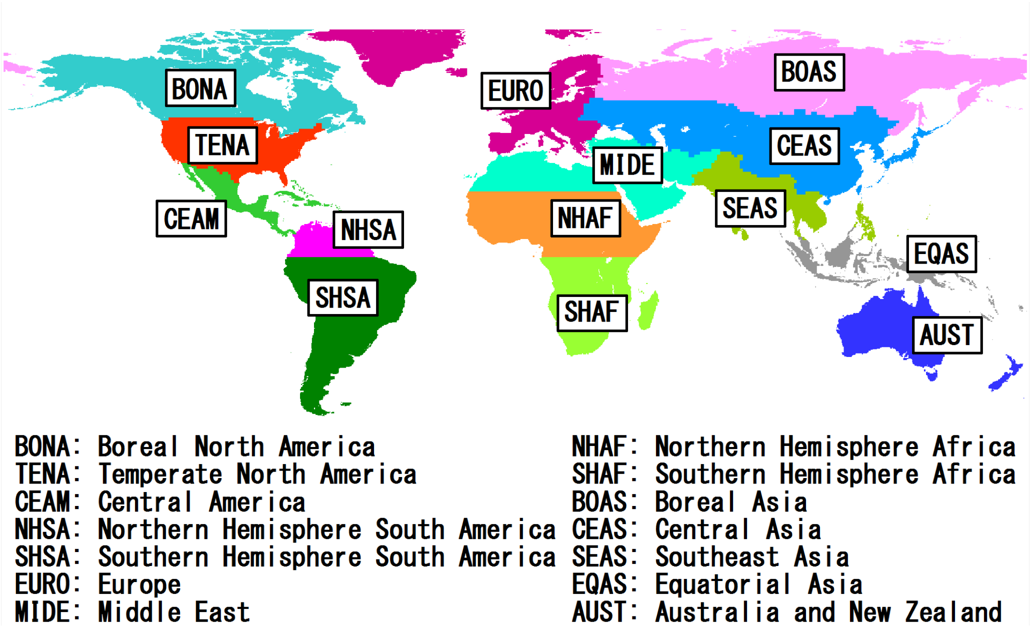

Figure A1. Map of the 14 global regions derived from Giglio et al. (2006) and van der Werf et al. (2017).

https://doi.org/10.5194/bg-2021-130
Preprint. Discussion started: 10 June 2021

Table A1. BE and EF of CO (g CO kg^{-1}) for the LCC types used in GLC2000. See Fig. A1 for abbreviations of the 14 global regions. Letters in brackets show corresponding biome types from van der Werf et al. (2017); A: Boreal forest; B: Temperate forest; C: Tropical forest; D: Savanna; E: Peat; and F: Agriculture.

LCC	BE	EF in the 14 regions													
		BONE	TENA	CEAM	NHSA	SHSA	EURO	MIDE	NHAF	SHAF	BOAS	CEAS	SEAS	EQAS	AUST
Tree Cover, broadleaved, evergreen	0.25	127 (A)	88 (B)	93 (C)	93 (C)	93 (C)	88 (B)	93 (C)	93 (C)	93 (C)	127 (A)	88 (B)	93 (C)	210 (E)	88 (B)
Tree Cover, broadleaved, deciduous, closed	0.25	127 (A)	88 (B)	93 (C)	93 (C)	93 (C)	88 (B)	93 (C)	93 (C)	93 (C)	127 (A)	88 (B)	93 (C)	210 (E)	88 (B)
Tree Cover, broadleaved, deciduous, open	0.4	127 (A)	88 (B)	93 (C)	93 (C)	93 (C)	88 (B)	93 (C)	93 (C)	93 (C)	127 (A)	88 (B)	93 (C)	210 (E)	88 (B)
Tree Cover, needle-leaved, evergreen	0.25	127 (A)	88 (B)	93 (C)	93 (C)	93 (C)	88 (B)	93 (C)	93 (C)	93 (C)	127 (A)	88 (B)	93 (C)	210 (E)	88 (B)
Tree Cover, needle-leaved, deciduous	0.25	127 (A)	88 (B)	93 (C)	93 (C)	93 (C)	88 (B)	93 (C)	93 (C)	93 (C)	127 (A)	88 (B)	93 (C)	210 (E)	88 (B)
Tree Cover, mixed leaf type	0.25	127 (A)	88 (B)	93 (C)	93 (C)	93 (C)	88 (B)	93 (C)	93 (C)	93 (C)	127 (A)	88 (B)	93 (C)	210 (E)	88 (B)
Tree Cover, regularly flooded, fresh water	0	127 (A)	88 (B)	93 (C)	93 (C)	93 (C)	88 (B)	93 (C)	93 (C)	93 (C)	127 (A)	88 (B)	93 (C)	210 (E)	88 (B)
Tree Cover, regularly flooded, saline water	0	127 (A)	88 (B)	93 (C)	93 (C)	93 (C)	88 (B)	93 (C)	93 (C)	93 (C)	127 (A)	88 (B)	93 (C)	210 (E)	88 (B)
Mosaic: Tree Cover, Other natural vegetation	0.35	127 (A)	88 (B)	93 (C)	93 (C)	93 (C)	88 (B)	93 (C)	93 (C)	93 (C)	127 (A)	88 (B)	93 (C)	210 (E)	88 (B)
Tree Cover, burned	0	127 (A)	88 (B)	93 (C)	93 (C)	93 (C)	88 (B)	93 (C)	93 (C)	93 (C)	127 (A)	88 (B)	93 (C)	210 (E)	88 (B)
Shrub Cover, closed–open, evergreen	0.9	63 (D)	63 (D)	63 (D)	63 (D)	63 (D)	63 (D)	63 (D)	63 (D)	63 (D)	63 (D)	63 (D)	63 (D)	63 (D)	63 (D)
Shrub Cover, closed–open, deciduous	0.4	63 (D)	63 (D)	63 (D)	63 (D)	63 (D)	63 (D)	63 (D)	63 (D)	63 (D)	63 (D)	63 (D)	63 (D)	63 (D)	63 (D)
Herbaceous Cover, closed–open	0.9	63 (D)	63 (D)	63 (D)	63 (D)	63 (D)	63 (D)	63 (D)	63 (D)	63 (D)	63 (D)	63 (D)	63 (D)	63 (D)	63 (D)
Sparse herbaceous or sparse shrub cover	0.6	63 (D)	63 (D)	63 (D)	63 (D)	63 (D)	63 (D)	63 (D)	63 (D)	63 (D)	63 (D)	63 (D)	63 (D)	63 (D)	63 (D)
Regularly flooded shrub and/or herbaceous cover	0	63 (D)	63 (D)	63 (D)	63 (D)	63 (D)	63 (D)	63 (D)	63 (D)	63 (D)	63 (D)	63 (D)	63 (D)	63 (D)	63 (D)
Cultivated and managed areas	0.6	102 (F)	102 (F)	102 (F)	102 (F)	102 (F)	102 (F)	102 (F)	102 (F)	102 (F)	102 (F)	102 (F)	102 (F)	102 (F)	102 (F)
Mosaic: Cropland, Tree Cover, Other natural vegetation	0.8	102 (F)	102 (F)	102 (F)	102 (F)	102 (F)	102 (F)	102 (F)	102 (F)	102 (F)	102 (F)	102 (F)	102 (F)	102 (F)	102 (F)
Mosaic: Cropland, Shrub and/or grass cover	0.75	102 (F)	102 (F)	102 (F)	102 (F)	102 (F)	102 (F)	102 (F)	102 (F)	102 (F)	102 (F)	102 (F)	102 (F)	102 (F)	102 (F)
Bare Areas	0	0	0	0	0	0	0	0	0	0	0	0	0	0	0
Water Bodies	0	0	0	0	0	0	0	0	0	0	0	0	0	0	0
Snow and Ice	0	0	0	0	0	0	0	0	0	0	0	0	0	0	0
Artificial surfaces and associated areas	0	0	0	0	0	0	0	0	0	0	0	0	0	0	0
No data	0	0	0	0	0	0	0	0	0	0	0	0	0	0	0

https://doi.org/10.5194/bg-2021-130
Preprint. Discussion started: 10 June 2021

Table A2. As Table A1, but for the LCC types used in MCD12Q1.

LCC	BE	EF in 14 regions													
		BONE	TENA	CEAM	NHSA	SHSA	EURO	MIDE	NHAF	SHAF	BOAS	CEAS	SEAS	EQAS	AUST
Evergreen Needleleaf Forests	0.25	127 (A)	88 (B)	93 (C)	93 (C)	93 (C)	88 (B)	93 (C)	93 (C)	93 (C)	127 (A)	88 (B)	93 (C)	210 (E)	88 (B)
Evergreen Broadleaf Forests	0.25	127 (A)	88 (B)	93 (C)	93 (C)	93 (C)	88 (B)	93 (C)	93 (C)	93 (C)	127 (A)	88 (B)	93 (C)	210 (E)	88 (B)
Deciduous Needleleaf Forests	0.25	127 (A)	88 (B)	93 (C)	93 (C)	93 (C)	88 (B)	93 (C)	93 (C)	93 (C)	127 (A)	88 (B)	93 (C)	210 (E)	88 (B)
Deciduous Broadleaf Forests	0.25	127 (A)	88 (B)	93 (C)	93 (C)	93 (C)	88 (B)	93 (C)	93 (C)	93 (C)	127 (A)	88 (B)	93 (C)	210 (E)	88 (B)
Mixed Forests	0.25	127 (A)	88 (B)	93 (C)	93 (C)	93 (C)	88 (B)	93 (C)	93 (C)	93 (C)	127 (A)	88 (B)	93 (C)	210 (E)	88 (B)
Closed Shrublands	0.9	63 (D)	63 (D)	63 (D)	63 (D)	63 (D)	63 (D)	63 (D)	63 (D)	63 (D)	63 (D)	63 (D)	63 (D)	63 (D)	63 (D)
Open Shrublands	0.9	63 (D)	63 (D)	63 (D)	63 (D)	63 (D)	63 (D)	63 (D)	63 (D)	63 (D)	63 (D)	63 (D)	63 (D)	63 (D)	63 (D)
Woody Savannas	0.8	63 (D)	63 (D)	63 (D)	63 (D)	63 (D)	63 (D)	63 (D)	63 (D)	63 (D)	63 (D)	63 (D)	63 (D)	63 (D)	63 (D)
Savannas	0.8	63 (D)	63 (D)	63 (D)	63 (D)	63 (D)	63 (D)	63 (D)	63 (D)	63 (D)	63 (D)	63 (D)	63 (D)	63 (D)	63 (D)
Grassland	0.75	63 (D)	63 (D)	63 (D)	63 (D)	63 (D)	63 (D)	63 (D)	63 (D)	63 (D)	63 (D)	63 (D)	63 (D)	63 (D)	63 (D)
Permanent Wetlands	0	0	0	0	0	0	0	0	0	0	0	0	0	0	0
Croplands	0.8	102 (F)	102 (F)	102 (F)	102 (F)	102 (F)	102 (F)	102 (F)	102 (F)	102 (F)	102 (F)	102 (F)	102 (F)	102 (F)	102 (F)
Urban and Built-up Land	0	0	0	0	0	0	0	0	0	0	0	0	0	0	0
Cropland/Natural Vegetation Mosaics	0.8	102 (F)	102 (F)	102 (F)	102 (F)	102 (F)	102 (F)	102 (F)	102 (F)	102 (F)	102 (F)	102 (F)	102 (F)	102 (F)	102 (F)
Permanent Snow and Ice	0	0	0	0	0	0	0	0	0	0	0	0	0	0	0
Barren	0.75	63 (D)	63 (D)	63 (D)	63 (D)	63 (D)	63 (D)	63 (D)	63 (D)	63 (D)	63 (D)	63 (D)	63 (D)	63 (D)	63 (D)
Water Bodies	0	0	0	0	0	0	0	0	0	0	0	0	0	0	0